Journal of Catalysis 279 (2011) 12–26

Contents lists available at ScienceDirect

Journal of Catalysis

journal homepage: www.elsevier.com/locate/jcat

Microkinetic modeling of the NO + H_2 system on Pt/Al_2O_3 catalyst using temporal analysis of products

Ashok Kumar, Xiaolin Zheng, Michael P. Harold *, Vemuri Balakotaiah *

Department of Chemical and Biomolecular Engineering, University of Houston, TX 77204 – 4404, United States

ARTICLE INFO

Article history:
Received 13 August 2010
Revised 12 November 2010
Accepted 8 December 2010

Keywords:
NO_x
Hydrogen
Platinum
Lean NO_x trap
Microkinetic
Modeling
TAP

ABSTRACT

A systematic experimental and modeling study of the NO + H_2 reaction system on Pt/Al_2O_3 catalyst was carried out using temporal analysis of products (TAP). A microkinetic model was developed that explains the transient product distribution during various experimental TAP protocols. NO pulsing experiments show the inhibiting effect of oxygen poisoning and the kinetic limitations posed by N–O bond scission. The NO–H_2 pump–probe experiments demonstrate the effect of temperature, H_2/NO ratio ($\geqslant 1$), and pulse delay time between consecutive NO and H_2 pulses on N_2, N_2O, and NH_3 selectivity. The simulations reveal the competition between surface N–N recombination and N and/or NO reaction with H to form N_2 and NH_3, respectively. The developed mechanistic-based microkinetic model accounts for all of the experimental data including the aforementioned selectivity versus pulse delay trends.

© 2010 Elsevier Inc. All rights reserved.

1. Introduction

NO_x storage and reduction (NSR) is an emerging technology for NO_x emission abatement in lean burn gasoline and diesel engines. NSR consists of two stages of operations: storage and reduction. The first stage involves storage of NO_x on an alkaline earth oxide (BaO, CaO), mediated by precious metals (Pt, Rh), in the form of nitrate or nitrite. This is followed by injection of a rich pulse of a shorter duration to reduce the stored NO_x to a mixture of N_2, N_2O, and NH_3. This cycle is repeated continuously to achieve exhaust cycle-averaged NO_x conversion greater than 90%.

The development of predictive lean NO_x trap (LNT) models is essential to understand and improve the NSR technology. LNT models of varying complexity have been developed by a number of research groups as highlighted in the surveys of Guthenke et al. [1] and Roy and Baiker [2]. Global reaction models provide an assessment of spatio-temporal features while keeping the chemistry manageable. A global LNT model that was developed by Tuttlies et al. [3] was based on a shrinking core concept at the particle level to describe the chemistry. A similar model was used by Olsson et al. [4] to explain NO_x storage. Bhatia et al. [5] assumed fast and slow storage sites in their global kinetic model for the LNT. The model was able to predict the spatio-temporal concentration profiles of both reactants and products. Koci et al. [6] incorporated the effect of ceria and barium in their comprehensive global model of NSR. Recently, Bhatia et al. [7] used global kinetics and crystallite-scale details to explain the effect of Pt dispersion on the rate limiting regime and selectivity for $Pt/BaO/Al_2O_3$ catalyst.

A comprehensive understanding of NSR mechanism and kinetics ultimately requires a microkinetic description. Xu et al. [8,9] developed a microkinetic model for steady state NO reduction by H_2 in the presence of O_2. Larson et al. [10] also simulated the steady state NO_x reduction by H_2 and CO in the presence of O_2 using microkinetic formulation. Lindholm et al. [11] developed a detailed microkinetic model for the NSR in the presence of H_2O and CO_2. These more complex models are continuing to evolve as more detailed transient experiments are conducted to justify their development.

Temporal analysis of products (TAP) was developed by Gleaves and coworkers [12], and has been effective in understanding the kinetics of gas–solid catalytic reaction systems. TAP operates under the Knudsen diffusion transport regime, hence eliminating the complexity of mass transfer limitations. Since NSR is an inherently transient process, that makes TAP a particularly suitable tool for mechanistic and kinetic investigations of NSR. In our group, we have employed TAP to study NSR chemistry on Pt/Al_2O_3 and $Pt/BaO/Al_2O_3$ catalysts using NO pulse and NO–H_2 pump–probe experiments [13–15]. TAP was also coupled with isotopic labeling to gain understanding of spillover mechanisms and distribution of stored NO_x in the barium phase [16]. Recently, TAP was used to estimate the effective diffusivity of stored NO_x in the barium phase of $Pt/BaO/Al_2O_3$ [17].

* Corresponding authors.
E-mail addresses: mharold@uh.edu (M.P. Harold), bala@uh.edu (V. Balakotaiah).

0021-9517/$ - see front matter © 2010 Elsevier Inc. All rights reserved.
doi:10.1016/j.jcat.2010.12.006

Nomenclature

A	cross-section area of reactor (m^2)
A_i	pre-exponential factor for reaction i ($mol/m^3/s$)
$A_{i,f}$	pre-exponential factor for forward reaction i ($mol/m^3/s$)
$A_{i,r}$	pre-exponential factor for reverse reaction i ($mol/m^3/s$)
C_k	dimensionless gas concentration of species k
$\widehat{C}_k$	gas concentration of species k (mol/m^3 of void space)
C_o	reference gas concentration (mol/m^3 of void space)
C_{Pt}	concentration of exposed Pt sites (mol exposed Pt/m^3 of catalyst)
d	molecular diameter (m)
$D_{C,k}$	diffusivity of species k in catalyst phase (m^2/s)
$D_{I,k}$	diffusivity of species k in inert phase (m^2/s)
D_o	reference diffusivity (m^2/s)
e	sum of square error
$E_{i,f}$	activation energy of forward reaction i (J/mol)
$E_{i,r}$	activation energy of reverse reaction i (J/mol)
F_k	exit flux of gaseous species k (mol/s)
F^{Exp}	experimental values of exit flux (mol/s)
F^{Sim}	simulated values of exit flux (mol/s)
$J_{p,k}$	peak flux of area normalized exit flux profile of species k
$k_{i,f}$	forward rate constant for reaction i ($mol/m^3/s$)
$k_{i,r}$	reverse rate constant for reaction i ($mol/m^3/s$)
L_1	length of zone 1 (m)
L_2	length of zone 2 (m)
L_3	length of zone 3 (m)
L	length of reactor (m)
$M_{w,k}$	molecular weight of gaseous species k (g/mol or kg/mol)
N_A	Avogadro number
N_k	inlet pulse size for gaseous species k (mol/pulse)
N_o	reference inlet pulse size (mol/pulse)
n	coefficient of adsorption
p	pulse number
P	pressure (Pa)
R	universal gas constant (J/mol/K)
$R_{i,f}$	forward rate of reaction i ($mol/m^3/s$)
$R_{i,r}$	reverse rate of reaction i ($mol/m^3/s$)
$\mathscr{R}_{g,k}$	rate of formation of gaseous species k ($mol/m^3/s$)
$\mathscr{R}_{s,k}$	rate of formation of surface species k ($mol/m^3/s$)
$S_{0,k}$	sticking coefficient of gaseous species k at zero coverage
T	temperature (K)
t	dimensionless time
$t'_{p,k}$	peak time for exit flux profile for species k (s)
t'	time (s)
Δt_{Valve}	half of pulse valve opening time (s)
T	temperature (K)
w	weight for square error
x_1	axial coordinate in zone 1 (m)
x_2	axial coordinate in zone 2 (m)
x_3	axial coordinate in zone 3 (m)
z_1	dimensionless axial coordinate in zone 1
z_2	dimensionless axial coordinate in zone 2
z_3	dimensionless axial coordinate in zone 3

Greek letters

α_v	active Pt site per unit volume (mol/m^3)
ε_C	porosity in catalyst phase
ε_I	porosity in inert phase
δ_k	inlet pulse profile of gaseous species k
θ_k	surface coverage of species k
θ_v	vacant site coverage
λ	mean free path (m)
ϕ	constant (m^2/s $(g/mol/K)^{0.5}$)
τ_d	delay time (s)
τ_s	spacing time (s)
Γ	surface site density (mol exposed Pt/m^2 exposed Pt area)

TAP has been used by several researchers to estimate gas diffusivity in porous materials [18–23], active site concentration [24,25], adsorption and desorption rate constants [26], and reaction rate constants using first order kinetics [27]. Zou et al. [28,29] studied pulse gas transport in TAP system. Gleaves and coworkers [12] were the first to use exit flux moment analysis to estimate kinetic parameters of heterogeneous reaction systems. Later, a thin-zone reactor model [30] was developed to simplify the parameter estimation. In the limit, reactant conversion using a single Pt particle was studied in the reactor filled with inert particles [31]. Schuurman and Gleaves [32] compared the steady state and unsteady state kinetics of *n*-butane oxidation over VPO using the TAP-2 reactor. Constales et al. [33] used the global transfer matrix formulation for single pulse experiments. Feres et al. [34] used probability theory to explain the high reactivity of a single Pt particle in the reactor. Kondratenko and Pérez-Ramírez [35] modeled N_2O decomposition over steam activated Fe–silicate. Hong et al. [26] used COMSOL™ to study H_2 and CO adsorption on silica supported cobalt catalysts. Soick et al. [36] modeled methane oxidation using 11 species and 14 rate parameters for MgO supported Pt. Balcaen et al. [37] used transient multivariable non-linear regression to study oxidative dehydrogenation of propane over vanadia based catalyst.

In spite of the progress made to model gas–solid reactions in the TAP system, there is still a lack of studies focused on quantitative estimation of kinetic parameters for a non-linear reaction system on a multifunctional catalyst. The simplification of a non-linear system to linear system has a limited validity. The current study is the step to elucidate the effect of various operating parameters for a non-linear reaction system consisting of several surface and gas phase species. Here, we use multiple pulse experiments for NO pulsing and NO–H_2 pump–probe to estimate the key kinetic parameters for NO–H_2 system on Pt/Al_2O_3 catalyst. Further, effect of various parameters like NO–H_2 delay time, H_2/NO ratio, and temperature on the product selectivity is discussed. The implications of the findings on the NSR reaction system are discussed.

2. Experimental

2.1. Experimental description

A Generation-1 TAP reactor system was used following the methodologies described in more detail elsewhere [13]. Experiments were carried out on 1.52 wt.% Pt/Al_2O_3 powder catalyst having 30.4% Pt dispersion, 1.14 m^2 exposed Pt surface area per gram of catalyst, and 3.7 nm average Pt particle diameter. The catalyst sample was provided by BASF Catalyst LLC (Iselin, NJ). About 16.2 mg of catalyst, with a particle size of 50–100 μm and having about 2.3×10^{17} exposed Pt sites, was sandwiched between two sections of inert quartz particle zones in a cylindrical reactor of 42 mm long and 5.3 mm in diameter. The quartz particles were 125–150 μm in diameter. The approximate thickness of the catalyst zone is 1 mm, which is sufficiently thin to ensure isothermal operation.

In a typical experiment, catalyst was first oxidized by flowing oxygen over the reactor bed at 350 °C for 10 min. The oxidation was followed by reduction by multiple pulses of H_2 (typically,

50–100 pulses of H_2 of pulse size 5×10^{15} molecules/pulse) enough to reduce only the exposed Pt and not the alumina as well. The temperature of the catalyst zone was then decreased to the reaction temperature (150–350 °C). The components Ar or NO and/or H_2 were injected into the reactor using fast pulsing valves. Effluent species of Ar (m/e = 40), N_2 (m/e = 28), NO (m/e = 30), N_2O (m/e = 44), NH_3 (m/e = 16), H_2O (m/e = 18), and H_2 (m/e = 2) were monitored with a calibrated UTI 100C quadrupole mass spectrometer. The NH_3 signal was measured at m/e = 16 to avoid overlap with H_2O at m/e = 17. The gaseous species signals were calibrated with several hundred pulses on the quartz bed reactor. The inlet pulse sizes were calculated by measuring the pressure drop in an isochoric bulb for each gaseous species. The pulse size was correlated with the mass spectrometer signal using a calibration number. The calibration numbers for NH_3 and H_2O were estimated by N and O balances, respectively, for selected experiment on Pt/Al_2O_3 catalyst and used throughout the study. Typically, the mass balances with this approach closed within 10%. Two principal experimental types were carried out, and are described below.

2.2. NO Pulsing experimental results

NO pulsing experiments involve exposure of multiple pulses of NO on pre-reduced catalyst with fixed spacing time (τ_s). The typical size of NO pulse was 1.0×10^{16} molecules/pulse. The spacing time between consecutive NO pulses was kept at 4.0 s.

These experiments reveal the progressive uptake of NO, O, and N species on Pt and their effect on the evolution of N_2 and N_2O. NO uptake over Pt/Al_2O_3 in the temperature range 150–350 °C has been discussed by Kumar et al. [15] and Medhekar et al. [14] in detail. N_2 is produced during initial NO pulses at high temperature (350 °C) and its formation declines with prolonged NO exposure due to oxygen accumulation on the Pt surface. As the surface begins to be covered by oxygen, unreacted NO starts to appear in the effluent and breakthrough of NO is evident. The N_2O production goes through maxima at the point of NO breakthrough. At a lower temperature, NO uptake decreases, the formation of N_2 decreases and the NO breakthrough occurs at lower pulse number. At 150 °C, the formation of N_2 and N_2O is negligible due to the kinetic limited N–O bond scission. During the NO uptake experiments for the temperature range considered there is no production of O_2 and NO_2. Below ca. 400 °C the O_2 desorption is kinetically limited while gaseous NO_2 formation is thermodynamically limited under TAP conditions. This is in contrast to atmospheric bench scale NO oxidation studies on Pt/Al_2O_3 in which NO_2 is the major product. If NO_2 is introduced in the TAP reactor system, it readily decomposes to form NO, N_2, and O_2 [13,15,16].

2.3. NO–H_2 pump–probe experimental results

In NO–H_2 pump–probe experiments, pulses of NO and H_2 were sequentially fed to the catalyst. The duration between successive NO and H_2 pulses is the delay time (τ_d) while the time duration between consecutive H_2 and NO pulses is the spacing time (τ_s). In this study, τ_s was fixed at 4.0 s while τ_d was varied between 0.0 s and 4.0 s.

The NO–H_2 pump–probe experiment reveals the transient reaction between NO and H_2 which result in the product distribution that depends on the temperature, H_2/NO ratio, and the delay time between NO and H_2 pulses. Higher temperatures favor NO decomposition to produce surface N and O, while at lower temperatures, N–O bond scission is kinetically limited. At higher temperatures (350 °C), surface N combines to from N_2. H_2 present in the feed is effective in scavenging surface oxygen producing H_2O. In contrast, at lower temperatures (150 °C), H_2 reacts with surface NO forming NH_3 as a major product. Hence, N_2 has maximum selectivity at higher temperatures while NH_3 has higher selectivity at lower temperatures. Moreover, the N–O bond scission is enhanced by presence of the H adatoms [15], leading to N_2 and NH_3. The H_2/NO ratio is a critical parameter affecting the NH_3 and N_2 selectivity. A higher H_2/NO feed ratio (>2) leads to higher H surface concentration in proximity to NO or N molecules, resulting in NH_3 formation. For a smaller ratio of H_2/NO (<1.5), H_2 scavenges only the O deposited by NO decomposition forming H_2O. In addition to the temperature and H_2/NO feed ratio, the delay time between NO and H_2 has a crucial effect on the N_2 and NH_3 selectivity. A longer delay between NO and H_2 facilitates NO decomposition to occur on Pt to form N_2 and surface O that can be scavenged by H_2 pulse. A shorter delay enables an overlap of NO and H_2 on surface that leads to surface interaction of N or NO with H species to form NH_3. Hence, ammonia selectivity increases with increase in H_2/NO ratio and decrease in delay times and temperature.

3. Model development

3.1. Reactor model

The TAP reactor is a three-zone fixed-bed reactor (Fig. 1) operated under high vacuum conditions. The predominant gas transport process is Knudsen diffusion. This section summarizes the generalized model of the reactor. The assumptions for the model are

i. Convection effects are negligible in the reactor and Knudsen diffusion is the predominant transport process.
ii. Gas phase reactions do not take place.
iii. Constant physical properties.
iv. No radial temperature and concentration gradients in the reactor.
v. No heat or mass transfer limitations.
vi. Negligible diffusional gradients (or pore diffusional limitations) in the catalyst powder. In other words, all of the exposed Pt sites are equally accessible. For the catalyst particle size used this is considered a reasonable approximation.
vii. Uniform catalyst temperatures.

We used three-zone model for the analysis. A simpler and numerically inexpensive thin-zone model can also be used. There was evidence for concentration gradients along the axis of the reactor for NO adsorption in the catalyst zone. Therefore, we used a more general three-zone model.

The temperature of the reactor is measured in the catalyst zone. The reactor heater is wrapped around central section of the reactor, so the heating is not uniform along the reactor length. Moreover, there are heat losses from the inlet and exit end of the reactor. These factors lead to non-uniformity in the temperature along the reactor. The non-uniformity in temperature for the similar system was reported by Schuurman et al. [38]. In this study, we assumed the temperature along the reactor is same as the catalyst zone temperature; we will justify the uniform temperature

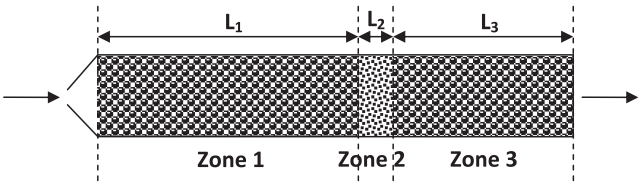

Fig. 1. Schematic of three-zone powder reactor. Catalyst is sandwiched between two sections of inert zones.

assumption in Section 3.2. The fluid phase species balances in two inert zones, zone 1 and zone 3, respectively, are given by

$$\frac{\partial \widehat{C}_k}{\partial t'} = D_{I,k}\frac{\partial^2 \widehat{C}_k}{\partial x_1^2}; \quad 0 < x_1 < L_1, \tag{1}$$

and

$$\frac{\partial \widehat{C}_k}{\partial t'} = D_{I,k}\frac{\partial^2 \widehat{C}_k}{\partial x_3^2}; \quad 0 < x_3 < L_3. \tag{2}$$

The fluid phase species balance of the sandwiched catalyst zone is given by

$$\frac{\partial \widehat{C}_k}{\partial t'} = D_{C,k}\frac{\partial^2 \widehat{C}_k}{\partial x_2^2} + \mathscr{R}_{g,k}\left(\frac{1-\varepsilon_C}{\varepsilon_C}\right); \quad 0 < x_2 < L_2, \tag{3}$$

and the surface species balance in the catalyst zone is given by

$$\frac{\partial \theta_k}{\partial t'} = \frac{\mathscr{R}_{s,k}}{C_{Pt}}, \tag{4}$$

with the constraint

$$\sum_k \theta_k + \theta_v = 1, \tag{5}$$

where the subscript v denotes the vacant sites and the summation is over all surface species. $\widehat{C}_k$ is the concentration (mol/m^3) of gas species k in the void space of inert beads or catalyst particles and θ_k is the fractional surface coverage of adsorbed species k. x_1, x_2, and x_3 are length scales (m) in zones 1, 2, and 3, respectively and t' is the time scale (s). L_1, L_2, and L_3 are lengths (m) of zones 1, 2, and 3 respectively. $D_{I,k}$ and $D_{C,k}$ are the diffusivities (m^2/s) of gaseous species k in inert and catalyst zones, and are assumed to be identical. The catalyst zone is very thin (~1 mm) compared to the reactor length (L). ε_I and ε_C are the bed porosity in the inert zones and catalyst zone, respectively. The measured values of porosity are similar. The rate of formation of gas phase species k, $\mathscr{R}_{g,k}$, and the rate of formation of surface species k, $\mathscr{R}_{s,k}$ are expressed in mol/m^3 catalyst/s. C_{Pt} is the exposed Pt surface concentration in mol Pt/m^3 catalyst. The reactor parameters used in this study is listed in Table 1.

Reactant or inert gases are pulsed into the reactor at $x_1 = 0$. The pulse width is 200–500 μs; this width is very small in comparison to diffusion time scale (~0.1 s), and hence the shape of inlet pulse (e.g. modified Gaussian or positive sinusoidal) does not affect the transient effluent shape. Even the pulse width interval does not change the effluent profiles as long as it is much smaller than the diffusion time scale. For the purpose of this study, we assume a positive sinusoidal pulse shape that is continuous and differentiable in the time interval of pulse width. A non-differential pulse shape like triangular or square pulse shape would cause steep flux gradients at the reactor inlet and would require smaller time steps for the numerical integration. In order to decrease computation time, those pulse shapes are avoided. The boundary condition at the inlet of reactor is defined as

$$-A\varepsilon_I D_{I,k}\left.\frac{\partial \widehat{C}_k}{\partial x_1}\right|_{x_1=0} = N_k\delta_k(t'), \tag{6}$$

where δ_k is the positive sinusoidal pulse. A is the cross sectional area of the reactor and N_k is the pulse size (mol/pulse) for species k. The outlet of the reactor is exposed to high vacuum of 10^{-8} torr. So, the concentration of gaseous species at the reactor exit is essentially zero, i.e.,

$$\widehat{C}_k|_{x_3=L_3} = 0. \tag{7}$$

In addition to the above inlet and outlet boundary conditions, the concentration and flux continuity are defined at the zones 1–2 interfacial boundary

$$\widehat{C}_k|_{x_1=L_1^-} = \widehat{C}_k|_{x_2=0^+}, \tag{8}$$

and

$$\varepsilon_I D_{I,k}\left.\frac{\partial \widehat{C}_k}{\partial x_1}\right|_{x_1=L_1^-} = \varepsilon_C D_{C,k}\left.\frac{\partial \widehat{C}_k}{\partial x_2}\right|_{x_2=0^+}. \tag{9}$$

Similarly, the gaseous concentration and flux continuity at the zones 2–3 interface are defined as

$$\widehat{C}_k|_{x_2=L_2^-} = \widehat{C}_k|_{x_3=0^+}, \tag{10}$$

and

$$\varepsilon_C D_{C,k}\left.\frac{\partial \widehat{C}_k}{\partial x}\right|_{x_2=L_2^-} = \varepsilon_I D_{I,k}\left.\frac{\partial \widehat{C}_k}{\partial x}\right|_{x_3=0^+}. \tag{11}$$

The concentration of gas and surface species in the reactor bed at the start of the pulse is equal to gas or surface concentration at the end of the previous cycle. The cycle time is τ_s for a pulsing experiment and $\tau_d + \tau_s$ for pump–probe experiment. As before, τ_s is the spacing time and τ_d is the delay time. The initial conditions for the gas concentration and surface concentration are

$$\widehat{C}_k|_{\substack{t'=0\\ pulse=p+1}} = \widehat{C}_k|_{\substack{t'=\tau_d+\tau_s\\ pulse=p}}, \tag{12}$$

and

$$\theta_k|_{\substack{t'=0\\ pulse=p+1}} = \theta_k|_{\substack{t'=\tau_d+\tau_s\\ pulse=p}}. \tag{13}$$

In addition to the calculation of gaseous and surface concentration profiles, the exit flux (mol/s) at the reactor outlet is calculated as

$$F_k = -A\varepsilon_I D_{I,k}\left.\frac{\partial \widehat{C}_k}{\partial x_3}\right|_{z_3=L_3}. \tag{14}$$

The above equations are non-dimensionalized using the following quantities

$$C_o = \frac{N_o}{A\varepsilon_I L}, \tag{15}$$

$$z_1 = \frac{x_1}{L}, \tag{16}$$

$$z_2 = \frac{L_1 + x_2}{L}, \tag{17}$$

$$z_3 = \frac{L_1 + L_2 + x_3}{L}, \tag{18}$$

$$t = \frac{t'}{L^2/D_o}, \tag{19}$$

Table 1
Properties and reactor parameters used in this study.

Parameter	Notation	Value
Length of zone 1	L_1	25 mm
Length of zone 2	L_2	1 mm
Length of zone 3	L_3	16 mm
Inert zone porosity	ε_I	0.4
Catalyst zone porosity	ε_C	0.4
Pt surface concentration	C_{Pt}	27.7 mol exposed Pt/m^3 catalyst
Cross section area of reactor	A	2.21×10^{-5} m^2
Surface site density	Γ	2.72×10^{-5} mol exposed Pt/m^2 exposed Pt

and

$$C_k = \frac{\widehat{C}_k}{C_o}. \tag{20}$$

Here, L is the length (m) of the reactor, C_o is the reference concentration (mol/m^3), N_o is reference pulse size (mol/pulse) and D_o is the reference diffusivity (m^2/s). z_1, z_2, and z_3 are dimensionless length scales for zones 1, 2, and 3, respectively, and t is the dimensionless time scale. Using the above expressions, the non-dimensionalized equations for zones 1, 2, and 3 are given by

Zone 1:

$$\frac{\partial C_k}{\partial t} = \frac{D_{I,k}}{D_o}\frac{\partial^2 C_k}{\partial_{x_1}^2}; \quad 0 < z_1 < \frac{L_1}{L}, \tag{21}$$

Zone 2:

$$\frac{\partial C_k}{\partial t} = \frac{D_{C,k}}{D_o}\frac{\partial^2 C_k}{\partial_{x_2}^2} + \mathscr{R}_{g,k}\frac{L^2}{C_o D_o}\left(\frac{1-\varepsilon_C}{\varepsilon_C}\right); \quad \frac{L_1}{L} < z_1 < \frac{L_1+L_2}{L}, \tag{22}$$

$$\frac{\partial \theta_k}{\partial t} = \frac{L^2 \mathscr{R}_{s,k}}{D_o C_{Pt}}, \tag{23}$$

with the constraint

$$\sum_k \theta_k + \theta_v = 1. \tag{24}$$

Zone 3:

$$\frac{\partial C_k}{\partial t} = \frac{D_{I,k}}{D_o}\frac{\partial^2 C_k}{\partial_{x_3}^2}; \frac{L_1+L_2}{L} < z_3 < 1. \tag{25}$$

Boundary conditions are as follows

Reactor inlet:

$$\left.\frac{\partial C_k}{\partial z_1}\right|_{z_1=0} = -\frac{D_o}{D_{I,k}}\frac{N_k}{N_o}\delta_k(t). \tag{26}$$

Here, $\delta_k(t)$ is defined for an inlet pulse as

$$\delta_k(t) = \frac{1}{2\Delta t_{Valve}}\left(1+\sin\left(\frac{\pi}{\Delta t_{Valve}}\left(t-\frac{\Delta t_{Valve}}{2}\right)\right)\right), \quad 0 \leqslant t \leqslant 2\Delta t_{Valve}, \tag{27}$$

or the finite Gaussian pulse

$$\delta_k(t) = \frac{1.3027}{\Delta t_{Valve}} e^{-\frac{4(t-\Delta t_{Valve})^2}{t(2\Delta t_{Valve}-t)}}, \quad 0 \leqslant t \leqslant 2\Delta t_{Valve}, \tag{28}$$

where Δt_{Value} is the half of dimensionless opening time of pulse valve. For this simulation, we used a positive sinusoidal response.

Zones 1–2 interface:

$$C_k|_{z_1=\frac{L_1^-}{L}} = C_k|_{z_2=\frac{L_1^+}{L}}, \tag{29}$$

and

$$\left.\frac{\partial C_k}{\partial z_1}\right|_{z_1=\frac{L_1^-}{L}} = \frac{\varepsilon_C D_{C,k}}{\varepsilon_I D_{I,k}}\left.\frac{\partial C_k}{\partial z_2}\right|_{z_2=\frac{L_1^+}{L}}. \tag{30}$$

Zones 2–3 interface:

$$C_k|_{z_2=\frac{L_1+L_2^-}{L}} = C_k|_{z_3=\frac{L_1+L_2^+}{L}}, \tag{31}$$

$$\left.\frac{\partial C_k}{\partial z_2}\right|_{z_2=\frac{L_1+L_2^-}{L}} = \frac{\varepsilon_I D_{I,k}}{\varepsilon_C D_{C,k}}\left.\frac{\partial C_k}{\partial z_3}\right|_{z_3=\frac{L_1+L_2^+}{L}}. \tag{32}$$

Reactor exit:

$$C_k|_{z_3=1} = 0. \tag{33}$$

Initial conditions:

$$C_k|_{\substack{t=0\\ pulse=p+1}} = C_k|_{\substack{t=\frac{\tau_d+\tau_s}{L^2/D_o}\\ pulse=p}}, \tag{34}$$

and

$$\theta_k|_{\substack{t=0\\ pulse=p+1}} = \theta_k|_{\substack{t=\frac{\tau_d+\tau_s}{L^2/D_o}\\ pulse=p}}. \tag{35}$$

Finally, the exit flux of species k, F_k, can be calculated using

$$F_k = -A\varepsilon_I D_{I,k}\frac{C_o}{L}\left.\frac{\partial C_k}{\partial z_3}\right|_{z_3=1}. \tag{36}$$

3.2. Transport regime

The predominant transport process in the reactor is Knudsen diffusion. This implies that the mean free path of the gas molecules is greater than the characteristic catalyst particle diameter in the reactor. This type of transport regime rules out the possibility of gas–gas interactions inside the reactor, so the primary interactions taking place in the reactor are of the solid–gas variety. The pulses of Ar with inlet pulses of size 2×10^{15}–2×10^{16} molecules/pulse were fed to the three-zone reactor at 350 °C and the exit flux was recorded. The area normalized flux responses were identical for each pulse size. The similar identical area normalized profiles were also obtained for N_2 at 350 °C and Ar at 250 °C and 150 °C. This means that the pulse size (up to 2×10^{16} molecules/pulse) does not affect the area normalized pulse shape, which is a characteristic of Knudsen diffusion transport. Further, the peak time ($t'_{p,k}$) and area normalized peak flux ($J_{p,k}$) for each case results in $J_{p,k}\times t'_{p,k} = 0.31$. Hence, assumption of Knudsen diffusion for the above TAP model development is justified.

The temperature and molecular weight is related to Knudsen diffusivity as

$$D_k = \phi\sqrt{\frac{T}{M_{w,k}}}, \tag{37}$$

where ϕ is an empirical parameter that depends on bed porosity, tortuosity, particle size, etc. Gleaves et al. [39] derived an expression for the peak time ($t'_{p,k}$) dependence on the reactor length (L) and diffusivity (D_k) as

$$t'_{p,k} = \frac{L^2}{6D_k}. \tag{38}$$

From the above two equations, peak time correlates to $\sqrt{\frac{M_{w,k}}{T}}$ as follows

$$t'_{p,k} = \frac{L^2}{6\phi}\sqrt{\frac{M_{w,k}}{T}}. \tag{39}$$

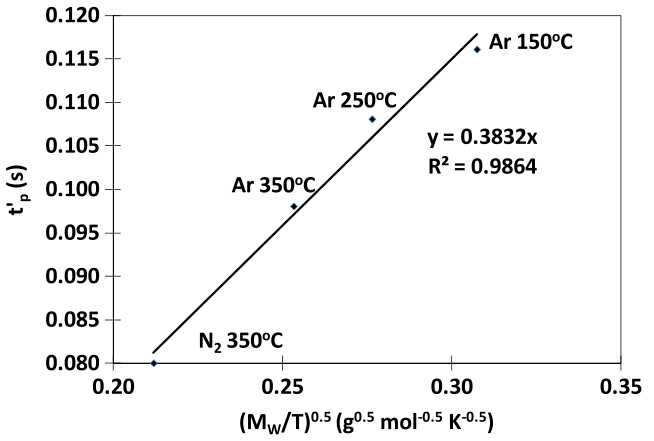

Fig. 2. Dependence of peak time on molecular weight and temperature for diffusivity estimation.

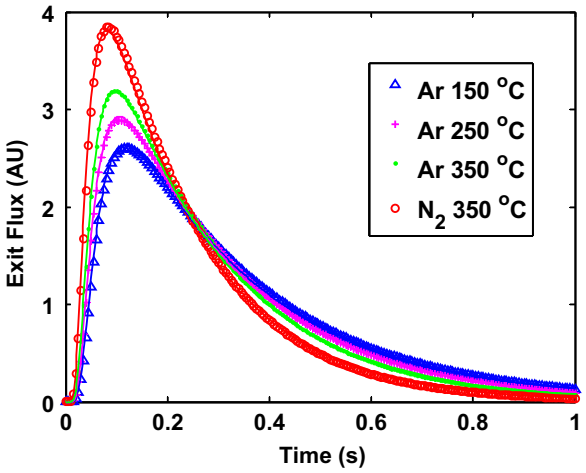

Fig. 3. Exit flux profiles for inert gases (Ar and N_2). The symbols are the experimental data and lines are simulation results throughout this paper.

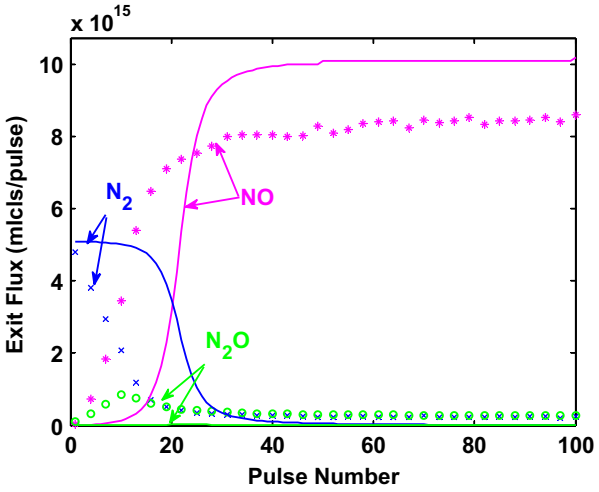

Fig. 4. Effluent integral profiles for NO pulsing at 350 °C, symbols are experimental data while lines are calculated using kinetic parameters from Xu et al. [9].

The value of ϕ from Fig. 2 is estimated as 7.77×10^{-4} m^2/s $(g/mol/K)^{0.5}$. This value is used to fit the transient diffusion curves for Ar at 150–350 °C and N_2 at 350 °C. The experimental transient curves fit very well with the simulated curves with the value of ϕ (Fig. 3). This value is used throughout this study for diffusivity estimation.

Although the temperature in the reactor is not uniform, the estimated diffusivity using a single temperature (measured in catalyst zone) is able to capture the exit flux profiles of inert species like N_2 and Ar (Fig. 3). For the case of reacting species in the Knudsen regime, the non-uniform temperature does not change the transport behavior. The non-uniform temperature can result in non-uniform gas–solid as well as gas–gas phase reaction rates. However, the quartz is an inert at the temperatures used, therefore, the gas–solid reactions are absent in the quartz zones. The gas–gas phase reactions are absent due to Knudsen transport conditions. The only reactions that occur are gas–solid reactions in the catalyst zone. Moreover, the temperature is measured in catalyst zone; therefore, the reaction rates are not affected by non-uniform temperature effects.

In addition to the uniform temperature assumption, we assumed constant diffusivity in the catalyst zone and inert zone. The nominal diameter of inert quartz particle is 125–150 μm while the catalyst particle size was less than 100 μm. The difference in the particle diameter results in difference in diffusivity in the inert zone and catalyst zone. The thickness of catalyst zone (~1 mm) is very small in comparison to reactor length (42 mm). A single uniform diffusivity in the reactor can explain the exit flux behavior for N_2 and Ar pulses in temperature range 150–350 °C (Fig. 3). Therefore, two different diffusivities, each for inert and catalyst zones, are not needed.

4. Modeling results and discussion

4.1. NO decomposition

NO decomposition experiments reveal the progressive uptake of NO, O, and N species on Pt and their effect on the evolution of N_2 and N_2O. NO decomposition at 250 and 350 °C involves stoichiometric formation of N_2 during the initial pulses followed by breakthrough of NO. The production of N_2O starts at zero, achieves a maximum during NO breakthrough, and then slowly decreases with pulse number (Fig. 4).

As described earlier, NO_2 and O_2 are not feasible products under TAP pressure and temperature conditions. The simplest microkinetic mechanism for N_2 and N_2O formation involves reversible NO adsorption, NO decomposition, N_2 formation, and N_2O formation. A four step mechanism with associated reaction rate parameters from Xu et al. [9] was used as a starting point. This was a subset of the larger microkinetic model for anaerobic NO reduction by H_2 on alumina-supported Pt. The model captured most experimental trends under steady state anaerobic conditions, particularly under rich conditions ($H_2/NO \geqslant 1$). In the NO decomposition submodel the formation of N_2 is considered as an irreversible reaction, while the reversible adsorption of NO is non-activated. The microkinetic mechanism for NO decomposition and the corresponding rate parameters used by Xu et al. [9] are provided in Table 2.

The integral profiles of N_2, NO, and N_2O predicted using the original kinetic parameters from Xu et al. [9] at 350 °C are shown in Fig. 4. During the first 15 pulses, the N_2 production is constant and unreacted NO in the effluent is negligible. The intersection of the NO and N_2 profiles occurs at the 20th pulse and the N_2O production is negligible over all the pulses. On the other hand, the experimental data have somewhat different trends. The data show a finite production of N_2O, gradual decrease in N_2 starting with the first pulse, and a gradual increase in effluent NO flux. Obviously, some tuning of the kinetic parameters and potential upgrade in the mechanism is needed to improve the simulation of the integral pulse data. A comparison of individual species flux response also showed the need for parameter tuning.

The next step involved a more rigorous fit of the model predictions to the transient species fluxes. A multi-response non-linear least squares algorithm was devised based on minimizing the least square sum of the objective function (e) between experimentally measured and simulated values of individual fluxes (mol/s). The objective function e

Table 2
Four step mechanism and rate constants for NO decomposition adopted from Xu et al. [9].

	Reaction	$A_{i,f}$ ($mol/m^3/s$)	$E_{i,f}$ (kJ/mol)	$A_{i,r}$ ($mol/m^3/s$)	$E_{i,r}$ (kJ/mol)
D1	NO + Pt ↔ NO–Pt	7.50×10^9		5.70×10^{17}	114.5
D2	NO–Pt + Pt ↔ N–Pt + O–Pt	5.44×10^{13}	107.8	4.00×10^{14}	128.1
D3	2 N–Pt → N_2 + 2Pt	4.00×10^{16}	130.0		
D4	NO–Pt + N–Pt ↔ N_2O + 2 Pt	4.02×10^{15}	85.7	2.00×10^8	24.0

$$e = \sum_{\text{Pulse number}} \sum_{\text{Temperature}} \sum_{\text{Gas species}} \sum_{\text{Time}} w(F^{\text{Exp}} - F^{\text{Sim}})^2. \quad (40)$$

The summation was over selected pulses of NO, N_2, and N_2O for initial 30 pulses; two temperatures 250 °C and 350 °C; three gas phase species and 390 data points per pulse transient. Though we collected experimental data with 1 ms interval, but for the simulation we use data points with 10 ms interval since it adequately capture the transient response of all species. In the above equation, w is the weight, F^{Exp} is the experimentally observed exit flux (mol/s), and F^{Sim} is the exit flux (mol/s) estimated by simulation. Specifically, the NO decomposition rate parameters were estimated for the individual transient pulses of NO, N_2, and N_2O at 250 and 350 °C using initial guess values from Xu et al. [9]. Another choice of the objective function may be defined between experimentally measured and simulated values of integral fluxes (mol/pulse). That would not be a good choice because the simulated transient fluxes (mol/s) may not necessary match to the experimentally measured transient fluxes though the integral fluxes (mol/pulse) are in good match. It is noted that pore diffusion limitations may have been present for some conditions, but the extent is likely not to be significant given the 50–100 μm particle size.

We used DLSODE to solve the system of PDE and ODRPACK 2.01 to optimize the rate parameters. The weights were selected based on an inspection of the typical responses. The rationale was as follows. A typical effluent flux profile during the 0–4 s period showed NO and N_2 as the major effluent species while N_2O fluxes were much lower (Fig. 5). The fluxes of NO and N_2 were highest in 0–1 s range and decreased to the baseline level afterwards (Fig. 6). For this reason, a base weight 1 was assigned for the NO and N_2 fluxes in the 0–1 s interval and assigned a lower value of 0.2 afterwards. The N_2O flux was generally an order of magnitude smaller than the NO and N_2. Hence, a larger weight of 8 was assigned for N_2O in the 0–1 s interval, 2 in 1–2 s interval, and 1 in 2–4 s interval. Similar logic was used for weight assignment for NO pulsing experiment at 250 °C also. The weights are tabulated in Table 3. There are more formal ways for optimization for these transient multi-response curves like Bayesian multi-response minimization that would potentially better fit the data and does not require weight assignment.

The initial kinetic parameters optimization for NO decomposition experiment was tried using steps D1–D4. The optimized parameters were not able to simultaneously explain all the features of NO decomposition experiment listed above. Hence, a need

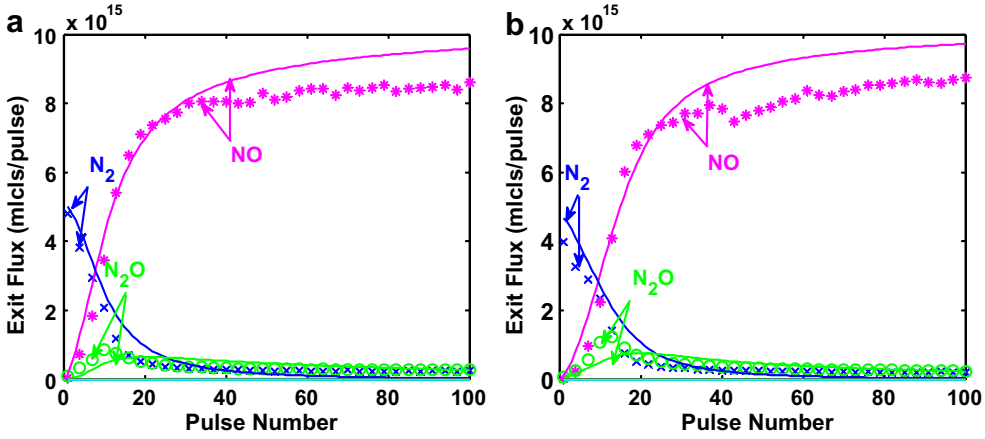

Fig. 5. NO decomposition on Pt/Al_2O_3 at 350 °C (a) and 250 °C (b). Symbols are experimental data while solid lines are simulation results throughout the paper.

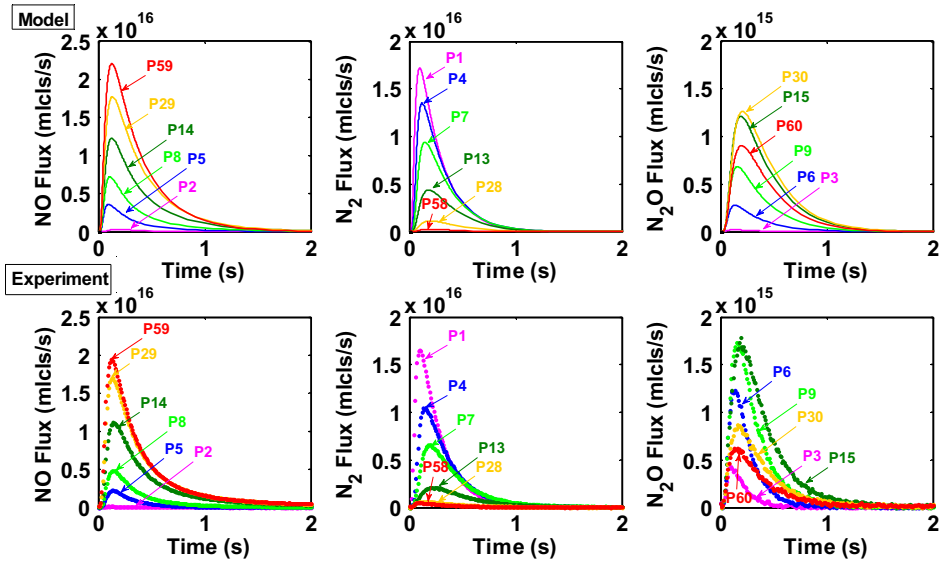

Fig. 6. Experimental and simulation results for individual transient pulse profiles for NO, N_2, and N_2O at 350 °C.

Table 3
Weights of individual flux responses for various temperatures, species, and transient time.

	250 °C			350 °C		
Time (s)	N_2	NO	N_2O	N_2	NO	N_2O
0.0–1.0	4	4	8	1	1	8
1.0–2.0	2	2	5	0.2	0.2	2
2.0–3.9	1	1	2	0.2	0.2	1

to change the reaction mechanism was realized. We added an additional reaction for N_2O formation; i.e. disproportionation of NO to form N_2O (Reaction D5). The resulting five-step reaction mechanism (D1–D5) is summarized in Table 4. The corresponding rate expressions are provided in Table 5. Here, $R_{i,f}$ and $R_{i,r}$ are the forward and reverse rates for reaction i, in mol/m^3/s.

In the parameter estimation the forward activation energies of steps D2 (adsorbed NO decomposition) and D3 (N_2 formation) were kept the same as those provided by Xu et al. [9]. We fixed the values of these activation energies in order to avoid convergence problems in the parameter estimation scheme. The NO desorption activation energy was fixed at 100.0 kJ/mol. This value is slightly lower than reported value of 114.5 kJ/mol [9]. A higher value of NO decomposition activation energy results in a sharper NO breakthrough and a sharper N_2 decrease. In addition, we used one enthalpy balance equation ($NO + NH_3 \leftrightarrow N_2O + 1½\ H_2$), that uses rate constants from the NO–H_2 reaction kinetics, to estimate the N_2O adsorption activation energy. This leads to three fixed parameters and 11 optimization parameters for the NO decomposition system.

The rate constant for adsorption of a species k, involved in reaction step i, is given by

$$k_i = S_{0,k}\alpha_v\sqrt{\frac{RT}{2\pi M_{w,k}}}, \tag{41}$$

where $S_{0,k}$ is the sticking coefficient of species k at zero coverage, R is the universal gas constant, T is temperature in K, $M_{w,k}$ is the molecular weight of species k in kg/mol and α_v is the active Pt surface area per unit volume of catalyst; α_v is calculated using

$$\alpha_v = \frac{C_{Pt}}{\Gamma}, \tag{42}$$

where C_{Pt} is the moles of Pt exposed per unit volume of catalyst and Γ is the surface site density in moles Pt per unit area of exposed Pt. The surface site density is an intrinsic parameter for a catalyst. We used a nominal value for Γ available in literature [40,41]. The rate of adsorption is given by

$$R_i = k_i\widehat{C}_k\theta_v^n, \tag{43}$$

where $\widehat{C}_k$ is the concentration (mol/m^3) of a gaseous species k in gas phase and θ_v is the fractional coverage of vacant Pt. The order of adsorption, n, is equal to 2 for second order adsorption and unity for first order adsorption. Here, we defined all the rate of reactions in terms of surface concentration and gaseous concentration. The Arrhenius rate expression was used for surface reactions, desorption and other adsorption reaction systems in which Eq. (41) was not used;

$$k_i = A_i e^{-\frac{E_i}{RT}}, \tag{44}$$

A_i is the pre-exponential factor and E_i is the activation energy (J/mol) for reaction step i.

The parameter estimation algorithm and upgraded microkinetic model for NO decomposition gave a much improved prediction of the experimental data. Fig. 5 shows the integral exit fluxes of N_2, NO, and N_2O with pulse number for NO decomposition at 350 °C and 250 °C. The five-step microkinetic mechanism with estimated rate constants is able to better capture and help us to elucidate the stoichiometric production of N_2 during initial pulse, NO breakthrough, and N_2O maxima. The additional route for N_2O formation (D5) by NO disproportionation reaction improves the N_2O prediction. Our simulation shows that NO disproportionation is the dominating route for N_2O formation.

The corresponding experimental and model predicted individual pulse responses of NO, N_2, and N_2O at 350 °C are shown in Fig. 6. The model predicts a N_2 flux profile that decreases with pulse number due to oxygen accumulation, and as a result the unreacted NO in the effluent increases with the pulse number. The model predicts reasonably well the peak flux, peak time, and their variation with the pulse number. Similar results of NO decomposition at 250 °C are shown in Fig. 7. The least square fit at 350 °C is somewhat better than that at 250 °C. At 250 °C, the spacing time between consecutive NO pulses was kept at 4.0 s and was insufficient for the gaseous NO concentration (or flux) to reach a baseline level. The experimental NO desorption profile has a protracted tail as does the N_2 and N_2O effluent profiles. The possible reasons may be that desorption of NO from Pt is slow and/or Al_2O_3 is also participating in the adsorption/desorption of NO. In the simulations, we accounted for the pulse not returning to the baseline level by using the instantaneous spatial profile as the initial condition for the next pulse.

In order to improve our understanding of the interaction of NO on Pt, we plot the exit fluxes of NO, N_2, and N_2O at 350 °C (Fig. 8). The surface coverages of adsorbed NO, N, and O as well as gaseous concentrations of NO, N_2, and N_2O are also plotted at the front of catalyst zone for pulses 1, 2, 5, 10, and 20. It is seen that the exit flux of N_2 is highest during the first pulse and decreases monotonically with pulse number. During this span of pulses, the fluxes of

Table 5
Rate expressions for NO decomposition on Pt.

i	Reaction	$R_{i,f}$ (mol/m^3/s)	$R_{i,r}$ (mol/m^3/s)
D1	NO + Pt ↔ NO–Pt	$k_{D1,f}\hat{C}_{NO}\theta_v$	$k_{D1,r}\theta_{NO}$
D2	NO–Pt + Pt ↔ N–Pt + O–Pt	$k_{D2,f}\theta_{NO}\theta_v$	$k_{D2,r}\theta_N\theta_O$
D3	2 N–Pt → N_2 + 2Pt	$k_{D3,f}\theta_N^2$	
D4	NO–Pt + N–Pt ↔ N_2O + 2 Pt	$k_{D4,f}\theta_{NO}\theta_N$	$k_{D4,r}\widehat{C}_{N_2O}\theta_v$
D5	2 NO–Pt → N_2O + O–Pt + Pt	$k_{D5,f}\theta_{NO}^2$	

Table 4
Rate parameters for NO decomposition on Pt. Underlined parameters were fixed, italicized parameter was calculated from enthalpy balance and others were optimized.

i	Reactions	$A_{i,f}$ (mol/m^3/s or s^{-1} (*))	$E_{i,f}$ (kJ/mol)	$A_{i,r}$ (mol/m^3/s or s^{-1} (*))	$E_{i,r}$ (kJ/mol)
D1	NO + Pt ↔ NO–Pt	$(2.38 \pm 0.19) \times 10^{8}$ (*)		$(2.45 \pm 0.9) \times 10^{16}$	<u>100.0</u>
D2	NO–Pt + Pt ↔ N–Pt + O–Pt	$(8.76 \pm 12.56) \times 10^{13}$	<u>107.8</u>	$(6.42 \pm 10.54) \times 10^{14}$	104.5 ± 5.0
D3	2 N–Pt → N_2 + 2Pt	$(2.71 \pm 1.17) \times 10^{16}$	<u>130.0</u>		
D4	NO–Pt + N–Pt ↔ N_2O + 2 Pt	$(3.69 \pm 0.2) \times 10^{9}$	81.5 ± 4.5	$(1.18 \pm 65.90) \times 10^{3}$ (*)	*36.2*
D5	2 NO–Pt → N_2O + O–Pt + Pt	$(6.45 \pm 0.6) \times 10^{15}$	152.1 ± 1.4		

(*) denotes the pre-exponential factors ($A_{i,f}$ and $A_{i,r}$) with unit s^{-1}.

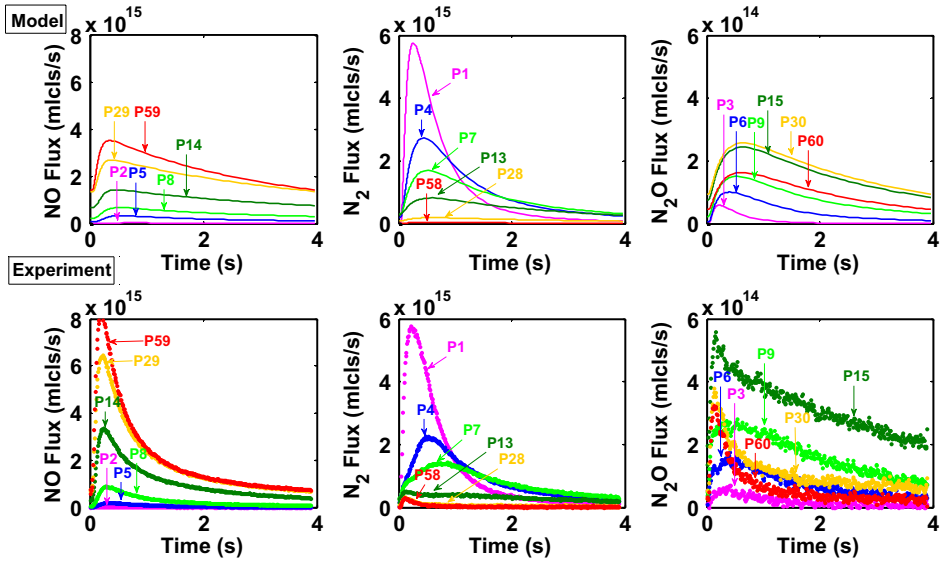

Fig. 7. Experimental and simulation results for individual transient pulse profiles for NO, N_2, and N_2O at 250 °C.

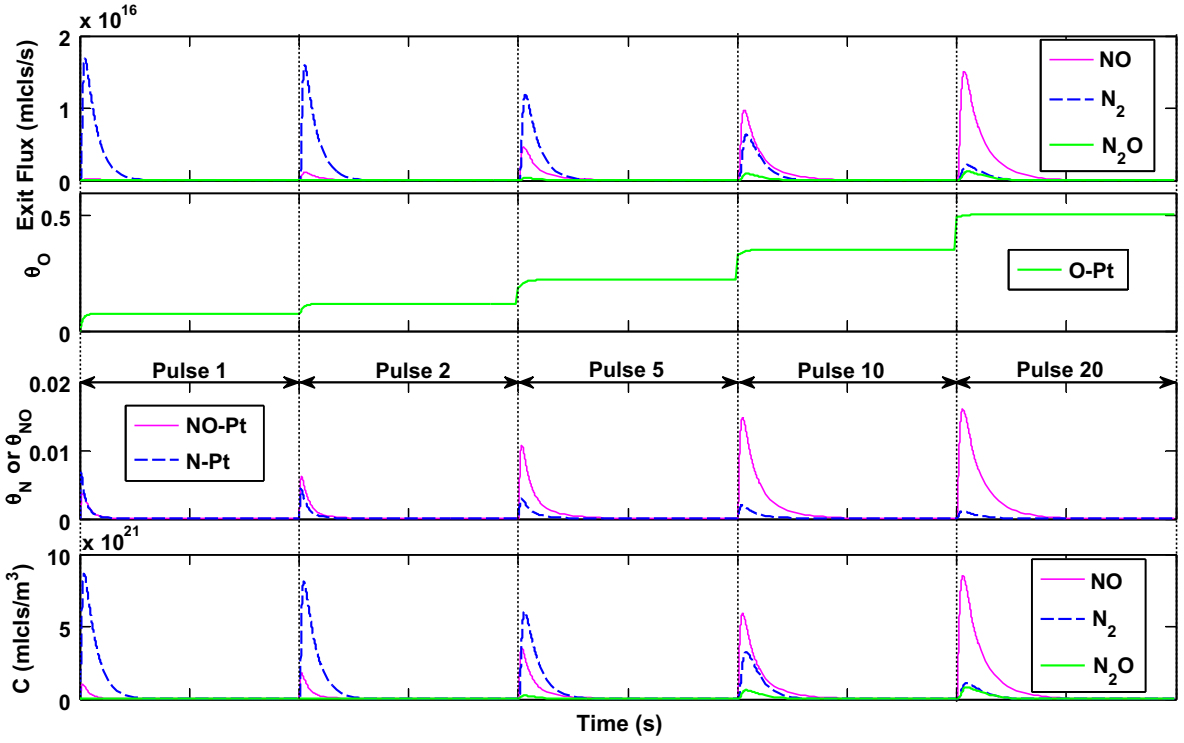

Fig. 8. Exit flux, surface coverage (θ), and concentration at front of catalyst zone for NO pulsing at 350 °C with pulse size 1.0×10^{16}.

NO and N_2O increase. By the 10th pulse, the NO flux surpasses that of N_2 and continues to grow. The surface coverages of adsorbed N and NO are negligible in comparison to adsorbed O at 350 °C. This shows that oxygen is the predominant species present on the Pt surface. The concentration profiles of gaseous species in the catalyst zone are similar to the exit flux profile.

The maximum gaseous concentration of any species for an inlet NO pulse of magnitude 1×10^{16} molecules/pulse is $\sim 10^{22}$ molecules/m^3. The total pressure of gases in the catalyst zone can be estimated by

$$P = \widehat{C}RT. \tag{45}$$

The above equation gives the maximum pressure in the catalyst zone to be about 86 Pa. The mean free path of the gaseous molecules (λ) in the packed bed reactor can be calculated as

$$\lambda = \frac{RT}{\sqrt{2}\pi d^2 N_A P}, \tag{46}$$

where d is the diameter of a gaseous molecule and N_A is Avogadro's number. The mean free path (λ) for a typical gas molecule of molecular diameter 0.3 nm at 350 °C is 250 μm. The value of the mean free path is greater than a typical catalyst powder size (~50 μm) and inert quartz particle (~125–150 μm). Hence, the assumption

of Knudsen diffusion for pulse size 10^{16} molecules/pulse is still valid. It has been already shown that the area normalized fluxes of N_2 and Ar coincide for the pulse size (<2×10^{16} molecules/pulse) and the temperatures below 350 °C. Moreover, the product $(J_{p,k} \times t'_{p,k})$ is equal to 0.31 and the calculated diffusivity explains well the exit flux profiles of inert gases confirms the Knudsen flow regime.

Finally, the current microkinetic mechanism of NO decomposition contains five steps. The mechanism involves three gas phase species (NO, N_2, and N_2O) and two elemental species (N and O). Further, the microkinetic formation of N_2 is assumed to be irreversible due to the very high adsorption activation energy of N_2. The thermodynamic constraint involves two gas phase species (NO and N_2O) with two elements (N and O). Hence, the NO decomposition reaction system does not require any thermodynamic constraint to be satisfied.

4.2. NO–H_2 pump–probe

The NO–H_2 pump probe experiments have a rich complexity of surface chemistry with multiple products formed. The experiments resulted in the formation of H_2O and NH_3 in addition to N_2 and N_2O. In this section, we discuss the effect of temperature, delay time and NO/H_2 ratio on product selectivity. The earlier study of Kumar et al. [15] provided related results to those reported here. However, the current data were used for the model simulations.

The three primary overall reactions between NO and H_2 are

$$NO + \frac{1}{2}H_2 \rightarrow \frac{1}{2}N_2O + \frac{1}{2}H_2O,$$

$$NO + H_2 \rightarrow \frac{1}{2}N_2 + H_2O, \quad \text{and}$$

$$NO + 2\frac{1}{2}H_2 \rightarrow NH_3 + H_2O.$$

The stoichiometric ratio of H_2 to NO is an important factor determining the formation of N_2O, N_2, or NH_3. We define the feed ratio $H_2/NO = 1$ for the production of N_2. Thus, for $H_2/NO < 1$, H_2 is the limiting reactant and NO is in excess; and for $H_2/NO > 1$, NO is the limiting reactant and H_2 is in excess.

The NO–H_2 pump–probe chemistry (P1–P9) involves H_2O and NH_3 formation in addition to N_2 and N_2O (Table 6). The corresponding rate expressions are described in Table 7. The kinetic parameters are as it is adopted from Xu et al. [9] with the following changes. The reaction (NH_3–Pt + 3 OH–Pt → N–Pt + 3 H_2O + 2 Pt) was eliminated because it overpredicts the formation of N_2 and the rate parameters for step P8 were modified to fit the N_2 and NH_3 integral profile. Here, for the case of NO–H_2 pump–probe chemistry on Pt, no further effort was made to optimize the kinetic parameter estimation.

Further, some of the reaction steps like ammonia formation (P5 and P6) and ammonia consumption (P8 and P9) are not elementary steps [9], but are steps that lump the sequential addition of H to the adsorbed NO or N and abstraction of H from surface ammonia.

NO–H_2 pump–probe involves formation of NH_3 and H_2O. The delayed appearance of these species suggests that NH_3 and H_2O adsorption/desorption is important. The adsorption of H_2O and NH_3 on Pt is not sufficient to explain the breakthrough of NH_3 and H_2O, so adsorption on Al_2O_3 (steps A1 and A2) had to be taken into account (Table 8). For NH_3 this is not surprising since it is basic while the γ-Al_2O_3 has acidic sites, so NH_3 readily adsorbs on Al_2O_3. Water as well has an affinity for the γ-Al_2O_3. Table 9 provides the rate expressions for H_2O and NH_3 adsorption on Al_2O_3. The surface area of Pt is 1.14 m^2/g of catalyst. For this catalyst sample, Pt is dispersed over high surface area γ-Al_2O_3 and the BET surface area of the catalyst is 100–120 m^2/g of catalyst. This means that the surface area of γ-Al_2O_3 is approximately 100 times that of the Pt surface area, hence we used surface concentration of Al_2O_3 sites as 100 times the concentration of Pt sites. The rate constant for adsorption of H_2O (step A1) and NH_3 (step A2) on γ-Al_2O_3 are given by

$$k_i = S_{0,k}(100\alpha_v)\sqrt{\frac{RT}{2\pi M_{w,k}}}. \tag{47}$$

Table 6
Rate parameters for NO–H_2 system on Pt.

i	Reaction	$A_{i,f}$ (mol/m^3/s) or S_0	$E_{i,f}$ (kJ/mol)	$A_{i,r}$ (mol/m^3/s) or S_0	$E_{i,r}$ (kJ/mol)
P1	H_2 + Pt ↔ 2 H–Pt	0.046		4.02×10^{14}	73.0
P2	H–Pt + O–Pt ↔ OH–Pt + Pt	4.02×10^{14}	11.5	6.28×10^{15}	74.9
P3	OH–Pt + H–Pt → H_2O + 2Pt	4.02×10^{14}	17.4		
P4	NO–Pt + H–Pt ↔ N–Pt + OH–Pt	4.02×10^{12}	60.0	4.60×10^{14}	143.7
P5	N–Pt + 3 H–Pt ↔ NH_3–Pt + 3 Pt	8.00×10^{14}	117.0	2.00×10^{17}	146.5
P6	NO–Pt + 3 H–Pt ↔ NH_3–Pt + O–Pt + 2 Pt	8.00×10^{14}	60.0	4.00×10^{15}	109.8
P7	NH_3–Pt ↔ NH_3 + Pt	8.50×10^{15}	48.4	1.00	
P8	NH_3–Pt + 3 O–Pt → N–Pt + 3 OH–Pt	1.00×10^{17}	80.0		
P9	NH_3–Pt + 3 NO–Pt + 3 Pt → 4 N–Pt + 3 OH–Pt	4.00×10^{14}	80.0		

Table 7
Rate expressions for NO–H_2 system on Pt.

i	Reaction	$R_{i,f}$ (mol/m^3/s)	$R_{i,r}$ (mol/m^3/s)
P1	H_2 + Pt ↔ 2 H–Pt	$k_{P1,f}\widehat{C}_{H_2}\theta_v$	$k_{P1,r}\theta_H^2$
P2	H–Pt + O–Pt ↔ OH–Pt + Pt	$k_{P2,f}\theta_H\theta_O$	$k_{P2,r}\theta_{OH}\theta_v$
P3	OH–Pt + H–Pt → H_2O + 2Pt	$k_{P3,f}\theta_{OH}\theta_H$	
P4	NO–Pt + H–Pt ↔ N–Pt + OH–Pt	$k_{P4,f}\theta_{NO}\theta_{OH}$	$k_{P4,r}\theta_N\theta_{OH}$
P5	N–Pt + 3 H–Pt ↔ NH_3–Pt + 3 Pt	$k_{P5,f}\theta_N\theta_H$	$k_{P5,r}\theta_{NH_3}\theta_v$
P6	NO–Pt + 3 H–Pt ↔ NH_3–Pt + O–Pt + 2 Pt	$k_{P6,f}\theta_{NO}\theta_H$	$k_{P6,r}\theta_{NH_3}\theta_O$
P7	NH_3–Pt ↔ NH_3 + Pt	$k_{P7,f}\theta_{NH_3}$	$k_{P7,r}\widehat{C}_{NH_3}\theta_v$
P8	NH_3–Pt + 3 O–Pt → N–Pt + 3 OH–Pt	$k_{P8,f}\theta_{NH_3}\theta_O$	
P9	NH_3–Pt + 3 NO–Pt + 3 Pt → 4 N–Pt + 3 OH–Pt	$k_{P9,f}\theta_{NH_3}\theta_{NO}$	

Table 8
Rate parameters for H_2O and NH_3 interactions on Al_2O_3.

i	Reaction	$S_{i,0}$	$E_{i,f}$ (kJ/mol)	$A_{i,r}$ (mol/m^3/s)	$E_{i,r}$ (kJ/mol)
A1	H_2O + Al_2O_3 ↔ H_2O–Al_2O_3	0.1		3.56×10^{11}	33.0
A2	NH_3 + Al_2O_3 ↔ NH_3–Al_2O_3	1.0		4.00×10^{14}	40.0

Table 9
Rate expressions for H_2O and NH_3 interactions on Al_2O_3.

i	Reaction	$R_{i,f}$ (mol/m^3/s)	$R_{i,r}$ (mol/m^3/s)
A1	H_2O + Al_2O_3 ↔ H_2O–Al_2O_3	$k_{A1,f}\widehat{C}_{H_2O}\theta_{v,Al_2O_3}$	$k_{A1,r}\theta_{H_2O,Al_2O_3}$
A2	NH_3 + Al_2O_3 ↔ NH_3–Al_2O_3	$k_{A2,f}\widehat{C}_{NH_3}\theta_{v,Al_2O_3}$	$k_{A2,r}\theta_{NH_3,Al_2O_3}$

The adsorption of H_2O and NH_3 on Al_2O_3 is inactivated. The sticking coefficient of 0.1 is used for water adsorption [42] and 1.0 is assumed for NH_3 adsorption. The desorption rate constants were estimated by fitting the H_2O and NH_3 profile for selected NO–H_2 pump–probe experiment that produce both H_2O and NH_3. These values of desorption constants are used throughout the study.

The experimental results show a delayed appearance of H_2O and NH_3 in the effluent. The integral response of H_2O and NH_3 shows a monotonic increase in their production, eventually approaching a saturation level. In order to match the integral trends of H_2O and NH_3, the saturated level values of H_2O and NH_3 during the NO–H_2 experiment were used as the inlet pulse sizes of H_2O and NH_3, respectively. The Pt chemistry was neglected for estimation of adsorption/desorption response on the Al_2O_3. The desorption rate constants for H_2O and NH_3 were estimated by integral responses of H_2O and NH_3 at 250 °C and 350 °C. The desorption rate constants were plotted against $\frac{1}{RT}$ to estimate activation energy of desorption and the pre-exponential factor (Table 8).

The NO–H_2 reaction system involves six gas phase species (NO, N_2, N_2O, NH_3, H_2O, and H_2) and three atomic species (N, O, and H). The formation of H_2O and N_2 are assumed to be irreversible. As a result, a thermodynamic analysis involves four gaseous species (NO, N_2O, NH_3, and H_2) and three elemental species (N, O, and H). This leaves one thermodynamic constraint for reaction ($NO + NH_3 \leftrightarrow N_2O + 1½\ H_2$), which has a heat of reaction of 35.91 kJ/mol. This reaction can be obtained by combining the steps

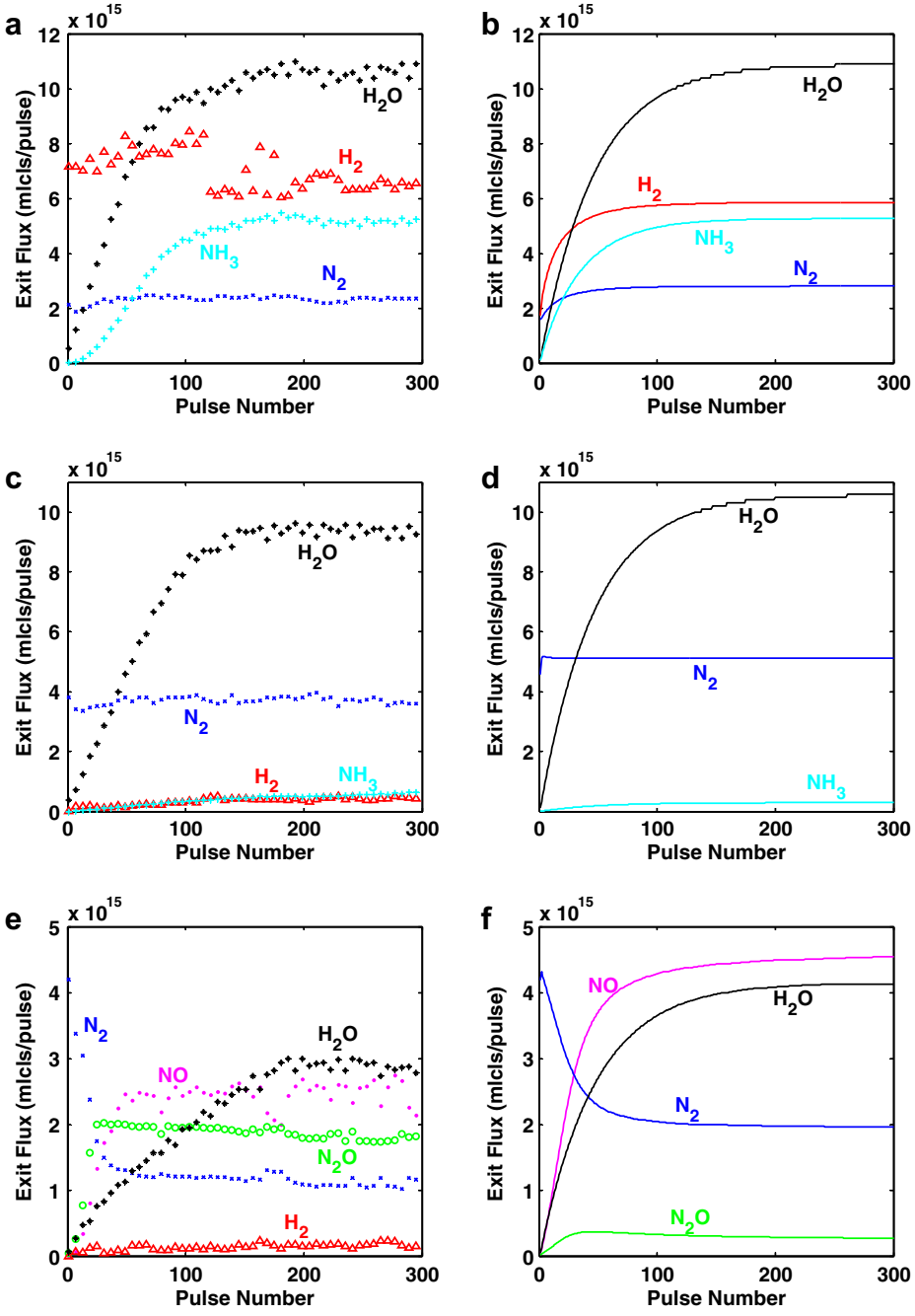

Fig. 9. Effect of H_2/NO ratio on product selectivity at 250 °C and 0.1 s delay time. (a and b) H_2/NO = 2.26, $NO_{In} = 1.09 \times 10^{16}$; (c and d) H_2/NO = 1.04, $NO_{In} = 1.06 \times 10^{16}$; (e and f) H_2/NO = 0.46, $NO_{In} = 0.90 \times 10^{16}$.

according to (D1 – P7 – P5 + D4 – 1½ P1). The activation energies listed in Table 4 and Table 6. Rate parameters for NO–H_2 system satisfies the enthalpy balance.

In addition to the enthalpic constraint, there is also an entropic constraint. The former affects the activation energies while the latter affects the pre-exponential factors for simple Arrhenius type rate expressions. Application of an entropic balance requires that each of the constituent reaction step is reversible and follows the mass action kinetics. Thus, for lumped reaction steps that are irreversible or do not follow mass action kinetics, entropic constraints cannot be applied.

Fig. 9 shows the experimentally measured effect of the H_2/NO ratio on the product selectivity of N_2O, N_2, and NH_3 at 250 °C and 0.1 s delay time. The H_2/NO ratio of 2.26 results in the predominant formation of NH_3 while N_2 being a byproduct. A lower ratio of 1.04 results in the predominant N_2 production and a small amount of NH_3 is also seen in the effluent. A further lower ratio of 0.46 results in formation of N_2 and N_2O. The H_2 is the limiting reactant so NO is also detected in the effluent.

The model comprising steps D1–D5 (Table 4), P1–P9 (Table 6) and A1–A2 (Table 8) predicts the predominant formation of NH_3 at H_2/NO ratio of 2.26 (Fig. 9a and b). The delayed appearance of H_2O and NH_3 is well captured. The N_2 remains at a sustained level. Since NO is a limiting reactant, it is not seen in the effluent. The H_2/NO stoichiometry does not favor the formation of N_2O, and it is well explained by the simulations. The model predicts the delayed appearance of H_2 in the effluent for excess of H_2 case, but the experimental data show a sustained unreacted H_2 in the exit. We do not have an explanation for this difference between model prediction and experiment.

The H_2/NO ratio of 1.04 results in the predominant formation of N_2 as well as a very small amount of NH_3 also produced (Fig. 9c and d). A smaller feed ratio of 0.46 leads to the formation of N_2 and N_2O as well as unreacted NO (Fig. 9e and f). The simulation predicts these trends. For example, the model predicts the stoichiometric formation of N_2 for the initial pulses and a declining N_2 production to a sustained value due to inhibition by surface oxygen. The model also predicts the breakthrough of NO and N_2O. The quantitative match for H_2/NO < 1 is not as good because the NO/H_2 rate parameters used in this study were taken from Xu et al. [9] and were quantitatively good for H_2/NO > 1.

Temperature is an important parameter affecting the product selectivity of N_2 and NH_3. Fig. 10 shows the experimentally observed effect of temperature for a fixed delay time of 0.1 s and H_2/NO ratio of 2.26–2.55. Higher temperature facilitates N–O bond scission on reduced Pt surface, forming gaseous N_2 and leaving O on the surface. A subsequent H_2 pulse, after a delay time of 0.1 s, scavenges the surface O to form H_2O. In comparison, at lower temperature, the rate of N–O bond scission is lower than at 350 °C. The higher interaction between NO or N with H leads to the increased formation of NH_3 at 250 °C.

Fig. 11 shows the experimentally measured effect of delay time on the selectivity of N_2 and NH_3 for a fixed temperature of 350 °C and H_2/NO ratio of 2.55. A shorter delay of ca. 0.0 s emulates a mixed feed in which NO and H_2 simultaneously enter the catalyst zone. With such a feed protocol the interaction between surface NO, N, and H are more prominent, leading to formation of NH_3. A longer delay between NO and H_2, e.g. 0.1 s, separates the NO and H_2 and the only way for these pulses to interact is through adsorbed O. As before, NO readily decomposes on Pt to form N_2,

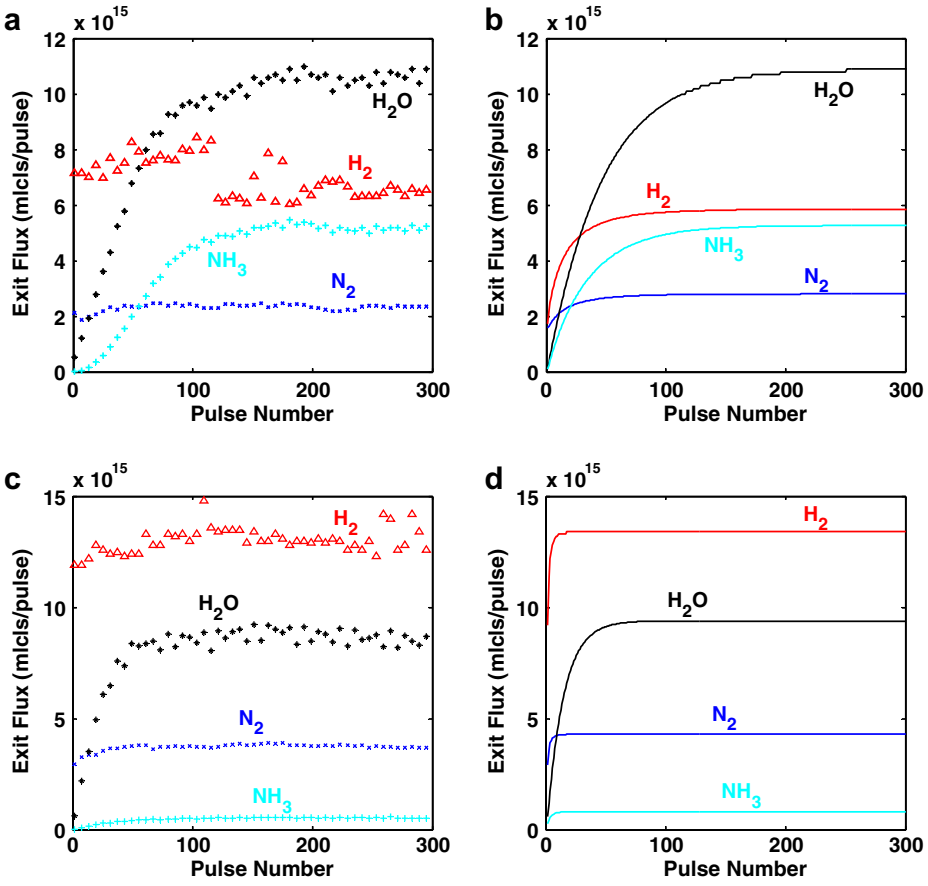

Fig. 10. Effect of temperature on product selectivity at 0.1 s delay time. (a and b) T = 250 °C, NO_{In} = 1.09 × 10^{16}, H_2/NO = 2.26; (c and d) T = 350 °C, NO_{In} = 0.94 × 10^{16}, H_2/NO = 2.55.

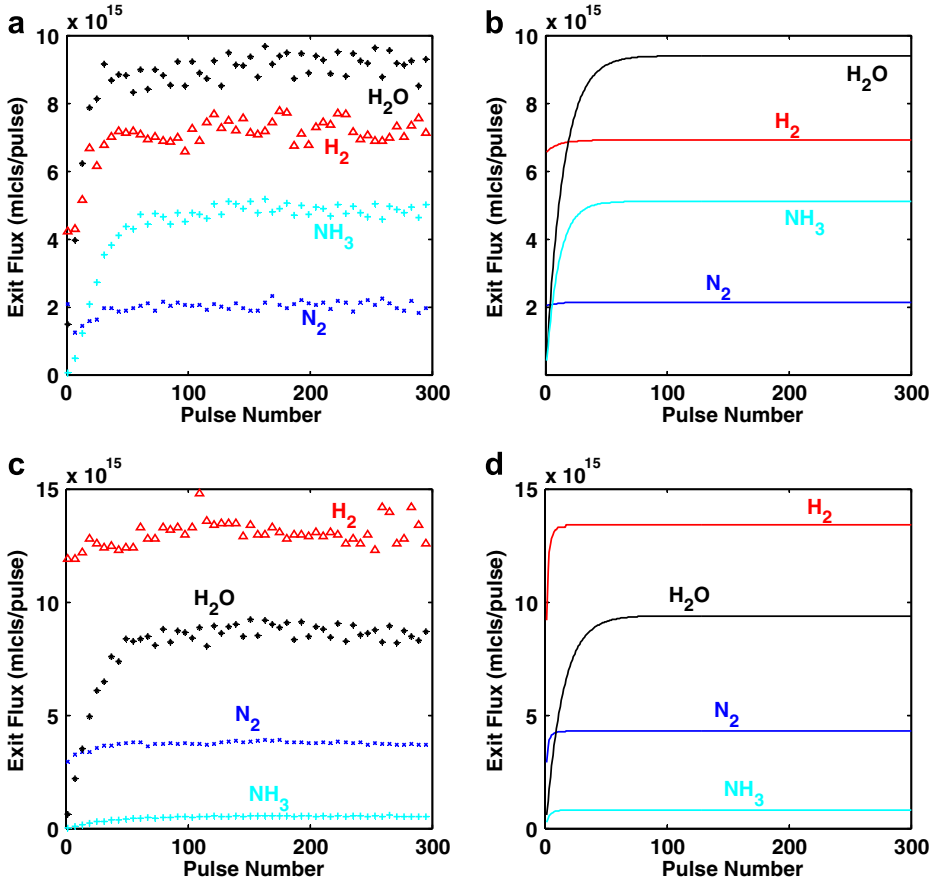

Fig. 11. Effect of delay time on product selectivity at 350 °C. (a and b) τ_d = 0.0 s, NO_{In} = 0.94 × 10^{16}, H_2/NO = 2.55; (c and d) τ_d = 0.1 s, NO_{In} = 0.94 × 10^{16}, H_2/NO = 2.55.

leaving surface O on the Pt. The subsequent H_2 pulse shows its presence on the Pt surface after a delay of 0.1 s. It scavenges the O from the surface, forming H_2O. As the delay time increases, the interaction between N and/or NO with H decreases. As a result, NH_3 formation decreases. The predominant route for N_2 formation for a longer delay time is solely due to NO decomposition. The formation of N_2 and NH_3 is a case of competition between N–N combination and combination of NO and/or N with H. The former produces N_2 while the latter facilitates the formation of NH_3.

A closer look at the effect of delay time is demonstrated by plotting the exit fluxes and surface and gas concentration at the front of the catalyst zone for delay times 0.0 s, 0.1 s, and 1.0 s (Fig. 12).

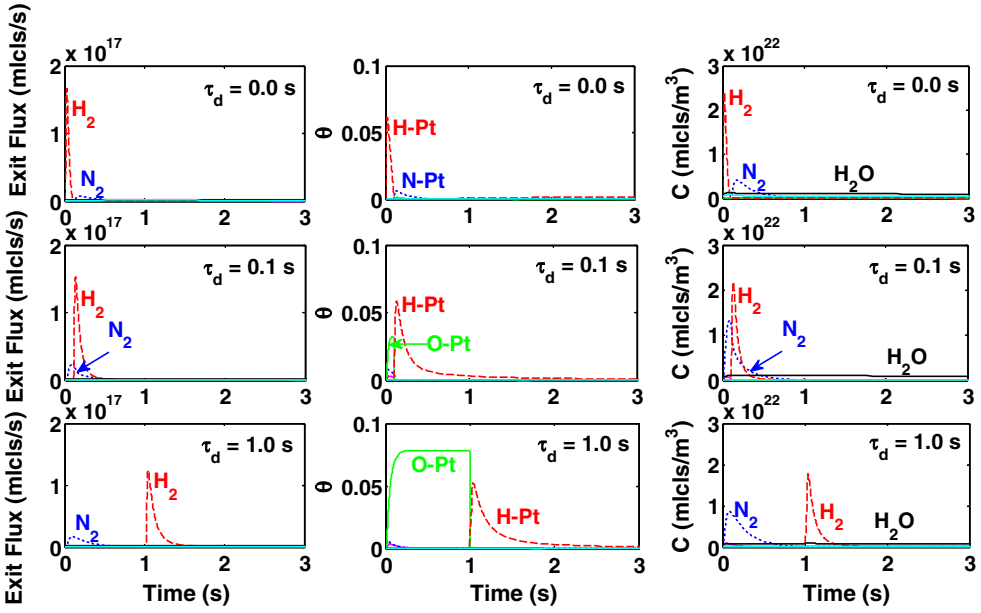

Fig. 12. Exit fluxes, surface coverages and gaseous concentrations at front of catalyst zone for NO–H_2 pump–probe at 50th pulse, 350 °C, H_2/NO = 2.5 and various delay times 0.0–1.0 s.

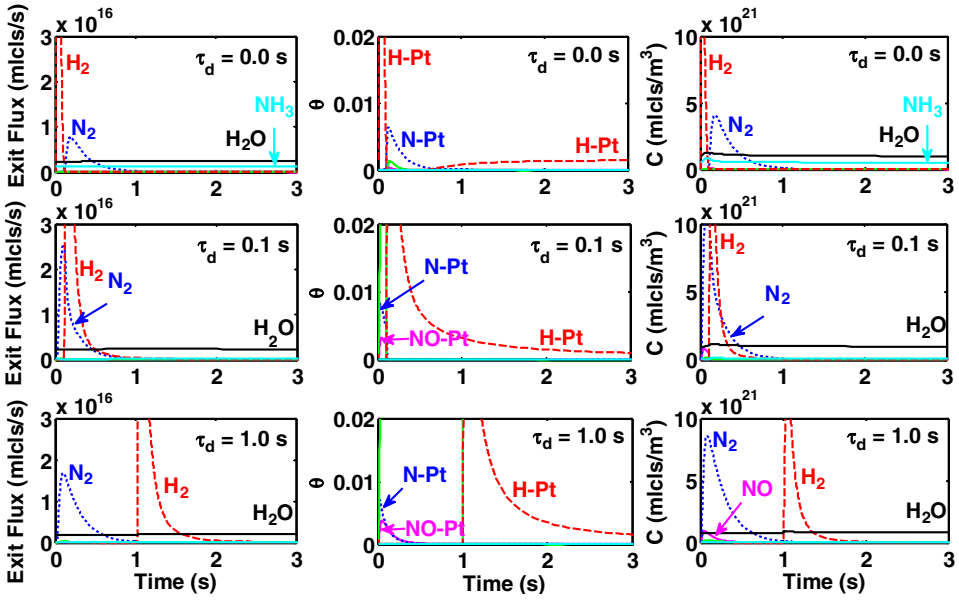

Fig. 13. Expanded view of Fig. 12. Exit fluxes, surface coverages and gaseous concentrations at front of catalyst zone for NO–H_2 pump–probe at 50th pulse, 350 °C, H_2/NO = 2.5 and various delay times 0.0–1.0 s.

An expanded view is provided in Fig. 13. The experimental conditions are 350 °C, H_2/NO = 2.5, and $NO_{In} = 1.0 \times 10^{16}$. The exit flux, surface concentration, and gaseous concentration profiles are plotted for the 50th NO–H_2 pump–probe cycle. With a longer delay time, τ_d = 1.0 s, the exit flux response shows formation of N_2 during the 0.0–1.0 s time interval. As seen in Fig. 12, the corresponding Pt surface shows a sharp increase in the O coverage due to oxygen produced by NO decomposition. There is very small coverage of NO and N at the point of NO pulsing but their coverages decrease with time due to NO decomposition and N_2 formation, respectively. The O coverage is sustained for 1.0 s because of absence of surface oxygen removal in the form of O_2, NO_2, etc. during that period. N_2 is the predominant gaseous species in the catalyst zone with traces of NO as depicted in the concentration profile plot. The catalyst zone shows a sustained level of H_2O which slowly desorbs from the Al_2O_3.

A successive pulse of H_2 at 1.0 s readily scavenges surface O as shown by the sudden decrease in oxygen coverage. The dominant species on the Pt is surface H. The concentration and flux profile also shows H_2 as the dominant species after 1.0 s. One point to note is that the delay between incoming NO and H_2 pulse is sufficiently long that NO and/or N_2 species does not overlap with H_2 in catalyst zone.

The exit flux and gas concentration profiles show that a smaller delay time of 0.1 s results in a larger overlap between N and H species. The N_2 flux and concentration profiles for 0.1 s delay are sharper and narrower than those for the 1.0 s delay. This is due to an enhancement of N_2 production due to surface reaction of surface NO and H (reaction step P4) in addition to NO decomposition. However, the integral amount of N_2 formation for a single NO–H_2 pump probe cycle is almost the same for 0.1 s and 1.0 s delay.

A further reduction in delay time to 0.0 s shows an overlap of the H_2 pulse by the NO pulse. Since, the Knudsen diffusivity of H_2 is 3.9 times that of NO, it transports faster through the catalyst bed than NO. Although NO and H_2 are fed simultaneously (more precisely, H_2 is delayed by 1.2 ms), H_2 overtakes NO in the inert zone and reaches the catalyst zone earlier than NO. The exit flux of N_2 at 0.0 s delay is smaller than that of 0.1 s or 1.0 s delay. In addition to the presence of H_2O, there is a sustained presence of NH_3 is seen in the catalyst zone. The surface coverage profile shows an interesting phenomenon: At the 0 s point, the H coverage shows a sharp peak due to H_2 dissociation, followed by increase in the N and O coverages due to NO decomposition. After this, there is sustained H coverage due to NH_3 decomposition.

The surface coverage shows a longer residence time for H than N during the τ_d to $\tau_d + \tau_s$ interval. The product of N recombination is N_2, which is an inert species. Once N_2 is formed, it does not readsorb on the Pt. On the other hand, H_2 formed by H–H combination can dissociatively readsorb on the Pt. Hence, the coverages of H are higher than N during τ_d to $\tau_d + \tau_s$ period.

A comprehensive plot (Fig. 14) shows that NH_3 selectivity is a sensitive function of temperature and delay time between NO and H_2 pulses. A mixed feed with delay time 0.0 s shows the highest selectivity of NH_3 formation. As the delay time increases, while keeping the temperature constant, the formation of NH_3 decreases. A longer delay time translates to a less pronounced overlap between NO and H_2 pulses on the catalyst, which leads to N_2 formation via N–N combination. For a shorter delay, N and/or NO

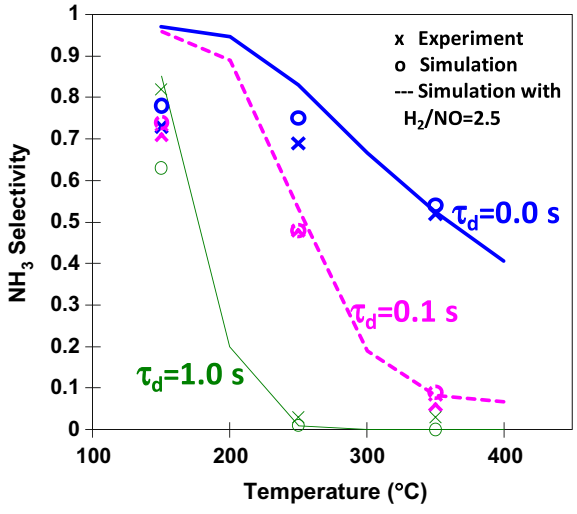

Fig. 14. NH_3 selectivity as function of temperature and delay times for H_2/NO = 2.0–2.5.

combines with surface H to form NH_3. Higher temperature also facilitates N_2 formation since, NO decomposition rates are higher and so does the N–N combination.

5. Conclusions

We have presented a comprehensive multi-pulse microkinetic model for NO decomposition and NO–H_2 pump–probe over Pt/Al_2O_3 catalyst that explains the essential experimental observations. NO pulsing experiments show the inhibition effect of oxygen poisoning in the studied temperature range. The NO–H_2 pump–probe experiments demonstrate the effect of temperature, H_2/NO ratio ($\geqslant 1$), and delay time between NO and H_2 pulses on N_2, N_2O, and NH_3 selectivity. The higher temperature favors NO decomposition to form N_2. The higher ratio of H_2/NO favors NH_3 production. A longer delay time between NO and H_2 would form N_2 as the dominant product while shorter delay time facilitates interaction between N and/or NO with H to form NH_3. The model also accounts for the physical adsorption/desorption on Al_2O_3. The model captures the competition between surface N–N recombination and N and/or NO reaction with H to form N_2 and NH_3, respectively.

Disclaimer

This report was prepared as an account of work sponsored by an agency of the United States Government. Neither the United States Government nor any agency thereof, nor any of their employees, makes any warranty, express or implied or assumes any legal liability or responsibility for the accuracy, completeness, or usefulness of any information, apparatus, product, or process disclosed, or represents that its use would not infringe privately owned rights. References herein to any specific commercial product, process, or service by trade name, trademark, manufacturer, or favoring by the United States Government or any agency thereof. The views and opinions of authors expressed herein do not necessarily state or reflect those of the United States Government or any agency thereof.

Acknowledgments

This study was jointly funded by BASF Catalysts LLC (formerly Engelhard Inc.) and the US DOE National Energy Technology Laboratory (DE-FC26-05NT 42630) with partial support from the National Science Foundation (CT 50730824).

References

[1] A. Güthenke, D. Chatterjee, M. Weibel, B. Krutzsch, P. Kocí, M. Marek, I. Nova, E. Tronconi, B.M. Guy, Advances in chemical engineering 33 (2008) 103.
[2] S. Roy, A. Baiker, Chemical Review 109 (2009) 4054–4091.
[3] U. Tuttlies, V. Schmeisser, G. Eigenberger, Chemical Engineering Science 59 (2004) 4731–4738.
[4] L. Olsson, R.J. Blint, E. Fridell, Industrial and Engineering Chemistry Research 44 (2005) 3021–3032.
[5] D. Bhatia, R.D. Clayton, M.P. Harold, V. Balakotaiah, Catalysis Today 147 (2009) S250.
[6] P. Kocí, F. Plát, J. Stepánek, S. Bártová, M. Marek, M. Kubícek, V. Schmeißer, D. Chatterjee, M. Weibel, Catalysis Today 147 (2009) S257.
[7] D. Bhatia, M.P. Harold, V. Balakotaiah, Catalysis Today 151 (2010) 314–329.
[8] J. Xu, R. Clayton, V. Balakotaiah, M.P. Harold, Applied Catalysis B: Environmental 77 (2008) 395–408.
[9] J. Xu, M.P. Harold, V. Balakotaiah, Applied Catalysis B: Environmental 89 (2009) 73.
[10] R.S. Larson, J.A. Pihl, V. Kalyana Chakravarthy, T.J. Toops, C.S. Daw, Catalysis Today 136 (2008) 104.
[11] A. Lindholm, N.W. Currier, J. Li, A. Yezerets, L. Olsson, Journal of Catalysis 258 (2008) 273.
[12] J.T. Gleaves, J.R. Ebner, T.C. Kuechler, Catalysis Reviews – Science and Engineering 30 (1988) 49–116.
[13] K.S. Kabin, P. Khanna, R.L. Muncrief, V. Medhekar, M.P. Harold, Catalysis Today 114 (2006) 72–85.
[14] V. Medhekar, V. Balakotaiah, M.P. Harold, Catalysis Today 121 (2007) 226–236.
[15] A. Kumar, V. Medhekar, M.P. Harold, V. Balakotaiah, Applied Catalysis B: Environmental 90 (2009) 642.
[16] A. Kumar, M.P. Harold, V. Balakotaiah, Journal of Catalysis 270 (2010) 214–223.
[17] A. Kumar, M.P. Harold, V. Balakotaiah, Industrial and Engineering Chemistry Research 49 (2010) 10334–10340.
[18] O.P. Keipert, M. Baerns, Chemical Engineering Science 53 (1998) 3623.
[19] T.A. Nijhuis, L.J.P. van den Broeke, M.J.G. Linders, J.M. van de Graaf, F. Kapteijn, M. Makkee, J.A. Moulijn, Chemical Engineering Science 54 (1999) 4423.
[20] J.A. Delgado, T.A. Nijhuis, F. Kapteijn, J.A. Moulijn, Chemical Engineering Science 59 (2004) 2477.
[21] W. Li, L. Xie, L. Gao, X. Zhao, R. Hu, Y. Cheng, D. Wang, Catalysis Today 121 (2007) 246.
[22] S.V. Nayak, M. Morali, P.A. Ramachandran, M.P. Dudukovic, Journal of Catalysis 266 (2009) 169.
[23] R.J. Berger, F. Kapteijn, J.A. Moulijn, G.B. Marin, J.D. Wilde, M. Olea, D. Chen, A. Holmen, L. Lietti, E. Tronconi, Y. Schuurman, Applied Catalysis A: General 342 (2008) 3–28.
[24] R. Hu, X. Zhao, S. Ding, W. Li, Y. Cheng, D. Wang, Chemical Engineering Science 62 (2007) 5317.
[25] Y. Schuurman, Catalysis Today 121 (2007) 187–196.
[26] J.J. Hong, S. Pietrzyk, A.Y. Khodakov, W. Chu, M. Olea, V. Balcaen, G.B. Marin, Applied Catalysis A: General 375 (2010) 116.
[27] G.S. Yablonsky, M. Olea, G.B. Marin, Journal of Catalysis 216 (2003) 120–134.
[28] B. Zou, M.P. Dudukovic, P.L. Mills, Chemical Engineering Science 48 (1993) 2345.
[29] B.S. Zou, M.P. Dudukovic, P.L. Mills, Journal of Catalysis 148 (1994) 683–696.
[30] S.O. Shekhtman, G.S. Yablonsky, S. Chen, J.T. Gleaves, Chemical Engineering Science 54 (1999) 4371–4378.
[31] X. Zheng, J.T. Gleaves, G.S. Yablonsky, T. Brownscombe, A. Gaffney, M. Clark, S. Han, Applied Catalysis A: General 341 (2008) 86–92.
[32] Y. Schuurman, J.T. Gleaves, Catalysis Today 33 (1997) 25.
[33] D. Constales, G.S. Yablonsky, G.B. Marin, J.T. Gleaves, Chemical Engineering Science 56 (2001) 133.
[34] R. Feres, A. Cloninger, G.S. Yablonsky, J.T. Gleaves, Chemical Engineering Science 64 (2009) 4358.
[35] E.V. Kondratenko, J. Pérez-Ramírez, Catalysis Today 121 (2007) 197.
[36] M. Soick, D. Wolf, M. Baerns, Chemical Engineering Science 55 (2000) 2875.
[37] V. Balcaen, I. Sack, M. Olea, G.B. Marin, Applied Catalysis A: General 371 (2009) 31–42.
[38] Y. Schuurman, Catalysis Today 138 (2008) 15.
[39] J.T. Gleaves, G.S. Yablonskii, P. Phanawadee, Y. Schuurman, Applied Catalysis A: General 160 (1997) 55–88.
[40] D. Chatterjee, O. Deutschmann, J. Warnatz, Faraday Discussions 119 (2001) 371–384.
[41] D. Bhatia, M.P. Harold, V. Balakotaiah, Chemical Engineering Science 64 (2009) 1544.
[42] J.W. Elam, C.E. Nelson, M.A. Cameron, M.A. Tolbert, S.M. George, Journal of Physical Chemistry B 102 (1998) 7008–7015.